Nano Research
2023, 16(7): 9371–9378

ISSN 1998-0124 CN 11-5974/O4
https://doi.org/10.1007/s12274-023-5578-1

Research Article

Engineering adjacent Fe_3C as proton-feeding centers to single Fe sites enabling boosted oxygen reduction reaction kinetics for robust Zn-air batteries at high current densities

Canhui Zhang, Xingkun Wang (✉), Kai Song, Kaiyue Chen, Shuixing Dai, Huanlei Wang, and Minghua Huang (✉)

School of Materials Science and Engineering, Ocean University of China, Qingdao 266100, China

Received: 1 February 2023 / **Revised:** 11 February 2023 / **Accepted:** 13 February 2023

ABSTRACT

Oxygen reduction reaction (ORR) plays an important role in the next-generation energy storage technologies, whereas it involves the sluggish and complicated proton-coupled electron transfer (PCET) steps that greatly limit the ORR kinetics. Therefore, it is urgent to construct an efficient catalyst that could simultaneously achieve the rapid oxygen-containing intermediates conversion and fast PCET process but remain challenging. Herein, the adjacent Fe_3C nanoparticles coupling with single Fe sites on the bubble-wrap-like porous N-doped carbon ($Fe_3C@Fe_{SA}$-NC) were deliberately constructed. Theoretical investigations reveal that the adjacent Fe_3C nanoparticles speed up the water dissociation and serve as proton-feeding centers for boosting the ORR kinetics of single Fe sites. Benefiting from the synergistic effect of the Fe_3C and single Fe sites, the $Fe_3C@Fe_{SA}$-NC affords an excellent half-wave potential of 0.88 V, and enables the assembled Zn-air batteries with the high peak power density of 164.5 mW·cm^{-2} and long-term stability of over 200 h at high current densities at 50 mA·cm^{-2}. This work clarifies the mechanism for improving ORR kinetics of single atomic sites by engineering the adjacent proton-feeding centers, shedding light on the rational design of cost-effective electrocatalysts for energy conversion and storage technologies.

KEYWORDS

oxygen reduction reaction, discharge stability, water dissociation, proton-coupled electron transfer

1 Introduction

The oxygen reduction reaction (ORR) has been recognized as an important section of the next energy conversion and storage technologies, such as Zn-air batteries (ZABs). Owing to the high theoretical energy density (1084 Wh·kg^{-1}), low-cost manufacturing, and environmental friendliness, ZABs are widely attracting attention [1–4]. However, the sluggish ORR occurred on the cathode greatly limits the ZABs performance [5–8]. To date, Pt-based materials are still regarded as benchmark ORR catalysts, but their high cost, poor long-term stability, and scarcity severely limited their large-scale commercialization. To address this challenge, the development of an efficient and robust electrocatalyst is essential to the further application of ZABs [9, 10].

In principle, the ORR usually proceeds the following electron transfer pathways: (1) $O_2(g) + * \rightarrow O_2*$; (2) $O_2* + H_2O(l) + e^- \rightarrow OOH* + OH^-$; (3) $OOH* + e^- \rightarrow O* + OH^-$; (4) $O* + H_2O(l) + e^- \rightarrow OH* + OH^-$; and (5) $OH* + e^- \rightarrow OH^- + *$, where * represents the active sites [11, 12]. Both the O_2* and O* need to couple with the protons from the water dissociation to generate the *OOH and *OH, which are frequently recognized as the proton-coupled electron transfer (PCET) steps [13, 14]. Therefore, the energy barrier of water dissociation and oxygen-containing intermediates conversion indubitably controls the proton-feeding kinetic rates and ORR performance, which are naturally taken into consideration for the rational design of cost-effective electrocatalysts [15–17]. To reduce these energy barriers, Xie's group constructed an electrocatalyst that engineers the sub-nano Pt nanoparticles on the surface-microenvironment-optimized Co_2N, in which the optimized surface microenvironment on Co_2N enables a boosted water dissociation process to facilitate PCET steps, thus achieving excellent ORR performance [18]. Feng and co-workers synthesized a nitrogen-doped hierarchically porous carbon with homogeneously distributed ultrafine α-MoC nanoparticles (α-MoC/NHPC), in which the α-MoC could reduce the energy barrier of the water dissociation and produce proton to accelerate the PCET process that could boost ORR kinetics of NHPC [19]. Consequently, constructing multiple sites in one system is a viable method to accelerate the proton-feeding kinetic rates and ORR performance.

Recently, single-atom catalysts (SACs), featuring their well-defined metal-N_4 (M-N_4) active sites, adjustable coordination structure, and impressive activities, are widely considered as the most promising candidate to the Pt-based catalysts in the field of electrocatalysis [20–23]. However, its obvious demerit, that is, only one kind of specific isolated active site, significantly limits the ORR activities by the linear scaling relations between the adsorption/desorption toward complicated multi-intermediates. Based on the above-mentioned considerations, we deliberately engineer the adjacent Fe_3C nanoparticles to single Fe sites on the bubble-wrap-like porous N-doped carbon ($Fe_3C@Fe_{SA}$-NC) [24, 25]. Density functional theory (DFT) unveils that the adjacent

Address correspondence to Xingkun Wang, xingkunwang@163.com; Minghua Huang, huangminghua@ouc.edu.cn

Fe_3C nanoparticles are in charge of the rapid water dissociation for achieving the fast PCET process, and the single Fe sites represent the rapid intermediates conversion, thus enabling the boosted proton-feeding kinetic rates and ORR performance. As a consequence, the $Fe_3C@Fe_{SA}$-NC affords an excellent half-wave potential of 0.88 V, and endows the assembled ZABs with a high peak power density of 164.5 mW·cm^{-2}. It is worth mentioning that the $Fe_3C@Fe_{SA}$-NC-based ZABs show excellent long-term stability at a high current density of 50 mA·cm^{-2} over 200 h, indicating the practical application ability of the catalyst. This work provides a rational design principle for the efficient ORR catalysts with accelerated catalytic kinetics via engineering adjacent proton-feeding centers to the single atomic sites.

2 Experimental section

2.1 Electrocatalysts preparation

The bubble-wrap-like porous carbon was synthesized by a freeze-drying and pyrolysis foaming process using sodium alginate as the carbon source. Then, a certain amount of $FeCl_3·6H_2O$ (5 mg·mL^{-1}) was introduced into the bubble-wrap-like porous carbon suspension under stirring. The powder was obtained by centrifuging with deionized water, and dried at 60 °C overnight in a vacuum oven. The obtained powder was ground with melamine and then carbonized to produce the $Fe_3C@Fe_{SA}$-NC at 900 °C for 180 min under the N_2 atmosphere. For comparison, the control Fe_{SA}-NC, NC, and pure carbon (C) catalysts were also synthesized with the similar procedure to that of the $Fe_3C@Fe_{SA}$-NC.

2.2 Characterizations

The morphology and structure of the obtained samples were characterized by scanning electron microscopy (SEM), transmission electron microscopy (TEM), high-resolution TEM (HRTEM), energy-dispersive X-ray spectroscopy (EDS), and atomic resolution aberration-corrected high-angle annular dark-field scanning TEM (AC HAADF-STEM). X-ray diffraction (XRD) patterns were noted by a Bruker D8 Advance diffractometer operated at 40 kV and 40 mA with a Cu Kα radiation (λ = 1.54178 Å). Raman spectroscopy was performed with a Thermo Fisher spectrometer equipped with helium-neon (633 nm) and argon (532 nm) lasers. X-ray photoelectron spectroscopy (XPS) was performed by Thermo ESCALAB 250XI.

2.3 Electrochemical measurements

The electrochemical measurements were implemented on CHI-842 electrochemical workstation at room temperature with the rotating disk electrode (RDE) or rotating ring-disk electrode (RRDE). 10 mg catalysts were dispersed into 1 mL mixed solution (N,N-dimethylformamide (DMF):isopropanol:5% Nafion = 4:1:0.1) and then ultrasonicated for 1 h to form the homogeneous catalyst ink. 9 μL catalysts ink was pipetted onto the working electrode (4 mm diameter) with the mass loading of 0.716 mg·cm^{-2}. The linear sweep voltammetry (LSV) was used to keep track of the ORR performance at the scan rate of 10 mV·s^{-1} in O_2-saturated 0.1 M KOH.

All potentials recorded in this work were converted to the reversible hydrogen electrode (RHE) according to the Nernst equation

$$E_{RHE} = E_{Ag/AgCl} + 0.197 + 0.059 \times pH$$

2.4 ZABs tests

The ZABs were assembled to evaluate the practical performance of the prepared samples. A polished Zn plate was used as the anode. The hydrophilic carbon paper coating with the catalyst layer (1 mg·cm^{-2}) was employed as air cathode and mixture solution of 6.0 M KOH + 0.2 M $Zn(Ac)_2·2H_2O$ served as the alkaline electrolyte. The LSV polarization curves of the alkaline ZABs were recorded on CHI-760 electrochemical workstation, and the galvanostatic discharge was performed at room temperature by a LAND testing system at 50 mA·cm^{-2}. For comparison, the alkaline Pt/C-based ZABs were assembled by using carbon paper coated commercial Pt/C catalyst as the air cathode.

3 Results and discussion

Figure 1(a) displays that a facile two-step pyrolysis method was adopted to prepare $Fe_3C@Fe_{SA}$-NC catalysts, in which the porous carbon was first synthesized via a seed-induced foaming approach, and then the $FeCl_3·6H_2O$ and melamine were introduced as the Fe and N source to yield the final $Fe_3C@Fe_{SA}$-NC catalyst at 900 °C [26]. Meanwhile, the Fe_{SA}-NC catalyst including only Fe single atoms was also synthesized for comparison. As presented in Fig. 1(b), and Figs. S1 and S2 in the Electronic Supplementary Material (ESM), SEM images of the $Fe_3C@Fe_{SA}$-NC catalyst reveal that it exhibits a similar "bubble-wraps" structure to the NC and pure C catalysts. This obtained carbon "bubble-wraps" structure could enable the catalysts with the "tree crown-stem" type porous skeleton accompanied with numerous micro/meso/macro-pores, which might be advantageous to speeding up the mass transfer of the reaction intermediates, and also exposing abundant accessible active sites to participate in the collision between the active sites and reaction intermediates, giving the boosted ORR performance [27]. Such a unique structure of the $Fe_3C@Fe_{SA}$-NC catalyst can be further demonstrated by its TEM image, as presented in Fig. 1(c). Besides, some nanoparticles with an average size of 13–25 nm can be clearly observed on the bubble-wrap-like porous N-doped carbon framework, manifesting that the Fe species was successfully introduced into the carbon substrate [28]. In order to investigate the detailed structural information of the $Fe_3C@Fe_{SA}$-NC catalyst, HRTEM and AC HAADF-STEM were employed. As shown in Fig. 1(d), a crystalline lattice distance of 0.21 nm can be obtained within the nanoparticles, which is traced to the (210) plane of the Fe_3C species. Moreover, the selected area electron diffraction (SAED) analysis was utilized to further prove the formation of the Fe_3C species. As displayed in Fig. S3 in the ESM, an obvious diffraction ring of (121) plane for the Fe_3C species can be captured, which supplies an additional evidence to confirm their existence [29]. The HAADF-STEM and corresponding elemental mapping images demonstrate the homogeneous distribution of the Fe, N, and C elements (Figs. 1(e)–1(h)). It can be clearly seen in AC HAADF-STEM images (Fig. 1(i)) that some single bright spots indexing the heavier Fe atoms (marked with red circles) are present around the nanoparticles, which evidently indicates the coexistence of the single Fe atom and Fe_3C species in the $Fe_3C@Fe_{SA}$-NC catalyst. As for the control Fe_{SA}-NC catalyst, no obvious particles can be found in the TEM (Fig. S4 in the ESM), and HAADF-STEM and corresponding elemental mapping images (Fig. S5 in the ESM), while there are only many single bright spots (marked by red cycles) can be captured in AC HAADF-STEM image (Fig. S6 in the ESM), strongly indicating the Fe species are mainly present as single atomic sites on carbon framework [30].

Figure 2(a) displays the XRD patterns of $Fe_3C@Fe_{SA}$-NC and Fe_{SA}-NC catalysts. The broad peaks at 24.0° and 44° attributed to the (002) plane of the graphitized carbon can be captured for the $Fe_3C@Fe_{SA}$-NC catalyst. Also, it presents some diffraction peaks at 38°, 43°, and 45° that are well-matched with the Fe_3C species (JCPDS #75-0910), indicative of the formation of Fe_3C in the

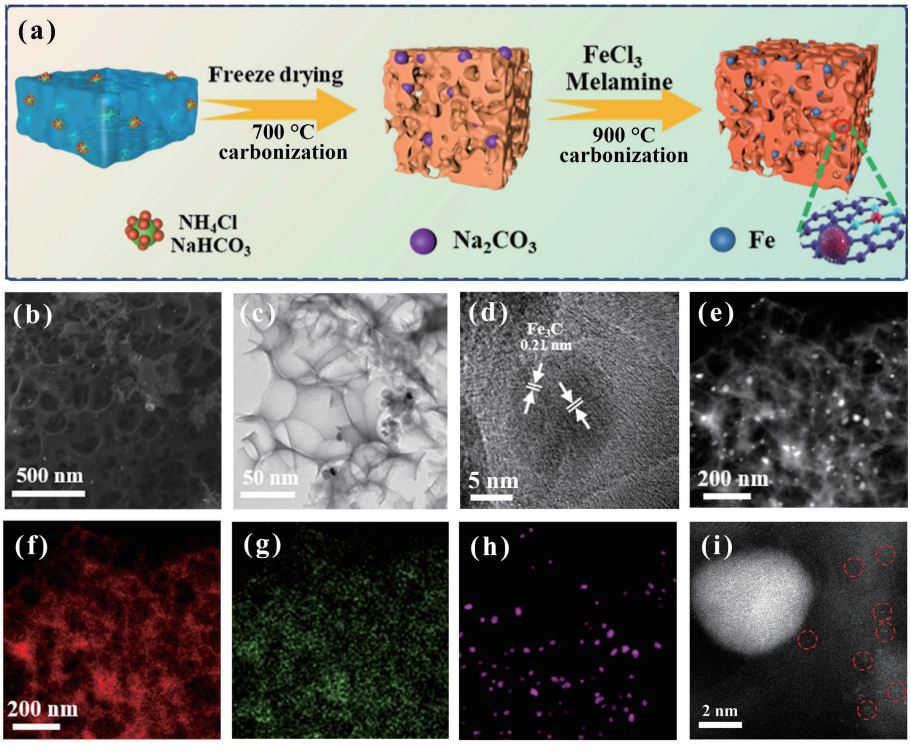

Figure 1 Morphological and structural characterization of the $Fe_3C@Fe_{SA}$-NC. (a) Schematic illustration of the synthesis process for $Fe_3C@Fe_{SA}$-NC. (b) SEM image, (c) TEM image, (d) HRTEM-STEM image, (e)–(h) elemental mapping images, and (i) AC HAADF-STEM image of the $Fe_3C@Fe_{SA}$-NC.

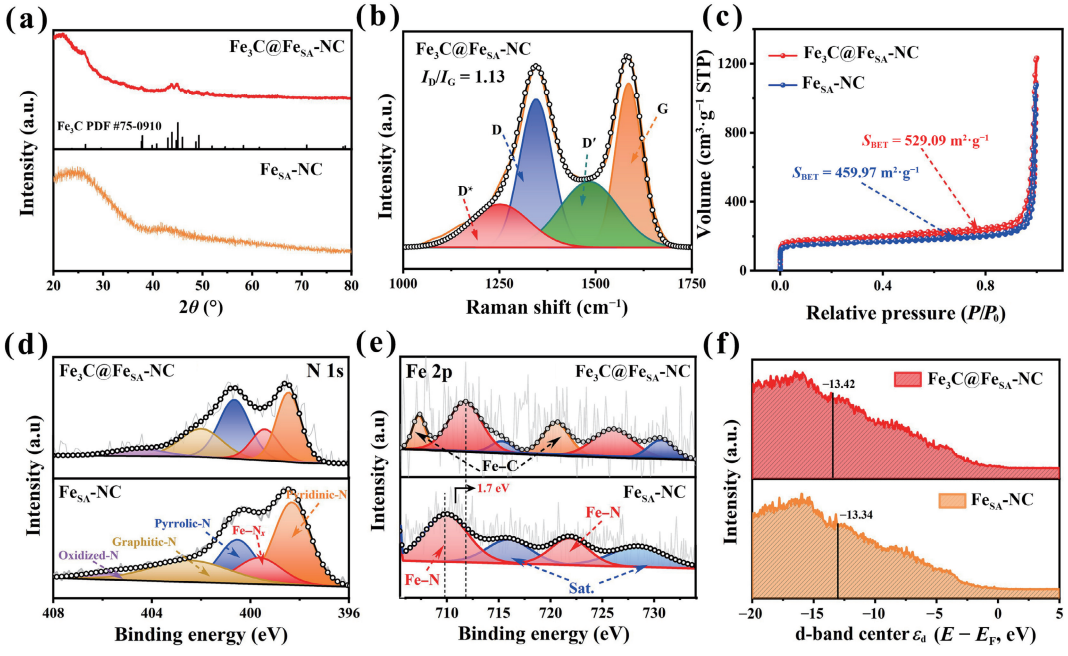

Figure 2 Structural and chemical identifications of $Fe_3C@Fe_{SA}$-NC. (a) XRD patterns of the $Fe_3C@Fe_{SA}$-NC and Fe_{SA}-NC catalyst. (b) Raman patterns of the $Fe_3C@Fe_{SA}$-NC. (c) Nitrogen adsorption–desorption isotherms of $Fe_3C@Fe_{SA}$-NC and Fe_{SA}-NC. (d) and (e) The N 1s and Fe 2p XPS spectra of the $Fe_3C@Fe_{SA}$-NC. (f) VBS of the $Fe_3C@Fe_{SA}$-NC and Fe_{SA}-NC.

$Fe_3C@Fe_{SA}$-NC catalyst [31, 32]. While the Fe_{SA}-NC catalysts only showcase the diffraction peaks belonging to the graphitized carbon, implying that no Fe-based nanoparticles are formed on the carbon framework. Raman spectroscopy was carried out to investigate the defects and graphitic structure of the obtained catalysts. As shown in Fig. 2(b) and Figs. S7–S10 in the ESM, two main typical peaks at 1344 and 1589 cm^{-1} assigned to the disordered carbon (D-band) and the sp^2 hybridization carbon (G-band) can be captured in the Raman spectra of the $Fe_3C@Fe_{SA}$-NC catalyst [33]. It can be seen that the $Fe_3C@Fe_{SA}$-NC catalyst pays the lowest intensity ratio of D to G band (1.13) among all investigated catalysts, unveiling that the introduction of Fe and N would increase the graphitization degree of the $Fe_3C@Fe_{SA}$-NC, which is generally accepted to be conducive to improving the conductivity and electron transfer ability for accomplishing the boosted ORR performance. N_2 adsorption/desorption isotherm was recorded to gain insight into the porous structure and surface area of the catalyst (Fig. 2(c)) [34]. The $Fe_3C@Fe_{SA}$-NC catalyst affords a higher Brunauer–Emmett–Teller (BET) surface area (529.09 $m^2 \cdot g^{-1}$) than the Fe_{SA}-NC catalyst (459.97 $m^2 \cdot g^{-1}$). The pore size distribution curves in Fig. S11 in the ESM decode the formation of hierarchical macro/meso/microporous structures in both the $Fe_3C@Fe_{SA}$-NC and Fe_{SA}-NC catalysts, which could effectively accelerate the mass transport of ORR intermediates and

expose more accessible active sites for participating the collision between the active sites and ORR intermediates, thus gaining the boosted ORR performance [35].

XPS was further employed to analyze the chemical states and compositions of catalysts [36, 37]. The XPS survey spectra of all catalysts reveal the existence of Fe, N, and C elements (Fig. S12 and Table S1 in the ESM). The C 1s spectra of $Fe_3C@Fe_{SA}$-NC in Figs. S13 and S14 in the ESM can be deconvoluted into C–C (284.1 eV), C–N (285.0 eV), C–OH (286.0 eV), and O–C=O (289.7 eV), respectively, in which the presence of C–N bond confirms the N is successfully incorporated into the carbon skeleton. As displayed in Fig. S15 in the ESM, the N 1s XPS spectra of NC catalyst display four peaks at 398.4, 400.6, 401.9, and 404.5 eV, which are attributed to the pyridinic-N, pyrrolic-N, graphitic-N, and oxidized-N species, respectively. As for both $Fe_3C@Fe_{SA}$-NC and Fe_{SA}-NC, Fig. 2(d) shows that addition peak indexing the Fe–N_x can be captured [38, 39]. Also, such Fe–N_x bond can be observed in the high-resolution Fe 2p XPS spectra of both $Fe_3C@Fe_{SA}$-NC and Fe_{SA}-NC (Fig. 2(e)), indicating the formation of single Fe atoms in them [40]. As shown in Fig. 2(e), the peaks at 706.9 and 720.3 eV are contributed to Fe–C bond for $Fe_3C@Fe_{SA}$-NC catalyst, decoding the formation of the Fe_3C species. These results again confirm the coexistence of the Fe_3C species and single Fe atoms in the $Fe_3C@Fe_{SA}$-NC catalyst. Significantly, it can be seen in Fig. 2(e) that the Fe–N_x species for the $Fe_3C@Fe_{SA}$-NC display a positive shift of 1.7 eV compared with that of the Fe_{SA}-NC, revealing that the strong electronic interaction is present between the Fe_3C species and single Fe atoms. As displayed in Fig. 2(f), the d-band center (ε_d) of the investigated catalysts was also calculated by the surface valence band spectra (VBS) [41, 42], in which the ε_d of the $Fe_3C@Fe_{SA}$-NC and Fe_{SA}-NC was determined to be −13.42 and −13.34 eV, respectively. These results suggest that the strong electronic interaction between Fe_3C species and single Fe atoms enables the catalysts with the down-shifted d-band center, thus resulting in the moderated bonding strength of the oxygen-related intermediates and boosted ORR activities [43, 44].

The electrocatalytic performance of $Fe_3C@FeSA$-NC was evaluated by the RDE measurement [45–47]. Cyclic voltammetry (CV) was first performed to assess the oxygen reactivity in 0.1 M KOH. As shown in Fig. S16 in the ESM, the $Fe_3C@Fe_{SA}$-NC exhibits the more positive peak than those of the Fe_{SA}-NC, NC, and pure C, implying its superior electrocatalytic properties toward ORR. LSV was further conducted to investigate the catalytic activity of the $Fe_3C@Fe_{SA}$-NC. As shown in Figs. 3(a)–3(c) and Table S2 in the ESM, the $Fe_3C@Fe_{SA}$-NC shows a higher half-wave potential ($E_{1/2}$ = 0.88 V) than the control Fe_{SA}-NC ($E_{1/2}$ = 0.82 V), NC ($E_{1/2}$ = 0.81 V), pure C ($E_{1/2}$ = 0.78 V), and Pt/C ($E_{1/2}$ = 0.85 V), which can be comparable to other previously reported ORR catalysts. Such strengthened ORR performance may be attributed to the synergistic effect of the single Fe atoms and Fe_3C species in the $Fe_3C@Fe_{SA}$-NC [48]. Figure 3(d) displays that the $Fe_3C@Fe_{SA}$-NC presents the lowest Tafel slope (49.71 mV·dec^{-1}) among all investigated catalysts, indicating its more favorable dynamic process toward ORR. Also, it exhibits a high kinetic current density (j_k) of 11.96 mA·cm^{-2} at 0.85 V, which was twice as high as that of the Pt/C (5.48 mA·cm^{-2}, Fig. 3(e)). The electrochemical active surface area of all catalysts was evaluated by the CV tests at different scan rates (Figs. S17–S21 in the ESM). It can be clearly seen that the $Fe_3C@Fe_{SA}$-NC affords the largest double-layer capacitance (C_{dl}) value of 126 mF·cm^{-2} for comparison with Fe_{SA}-NC (124 mF·cm^{-2}), NC (109 mF·cm^{-2}), and pure C (98 mF·cm^{-2}), implying more effective catalytic sites created on the $Fe_3C@Fe_{SA}$-NC. The electron transfer number (n) toward ORR was appraised by the RRDE measurement and is calculated to be 3.69 (close to 4), manifesting the ideal 4e$^-$ reduction process experienced (Fig. S22 in the ESM) [49]. The LSV curves recorded at different rotation rates from 400 to 2500 rpm were also studied to investigate the electron transfer number of $Fe_3C@Fe_{SA}$-NC. As shown in Fig. S23 in the ESM, the average number of $Fe_3C@Fe_{SA}$-NC can be extracted from the corresponding Koutechy–Levich (K–L) equation and determined to be 3.7–3.8, again decoding the ideal 4e$^-$ reduction process undergone. Besides, the electrochemical stability of $Fe_3C@Fe_{SA}$-NC during ORR was supported by the chronoamperometric measurements [50]. The

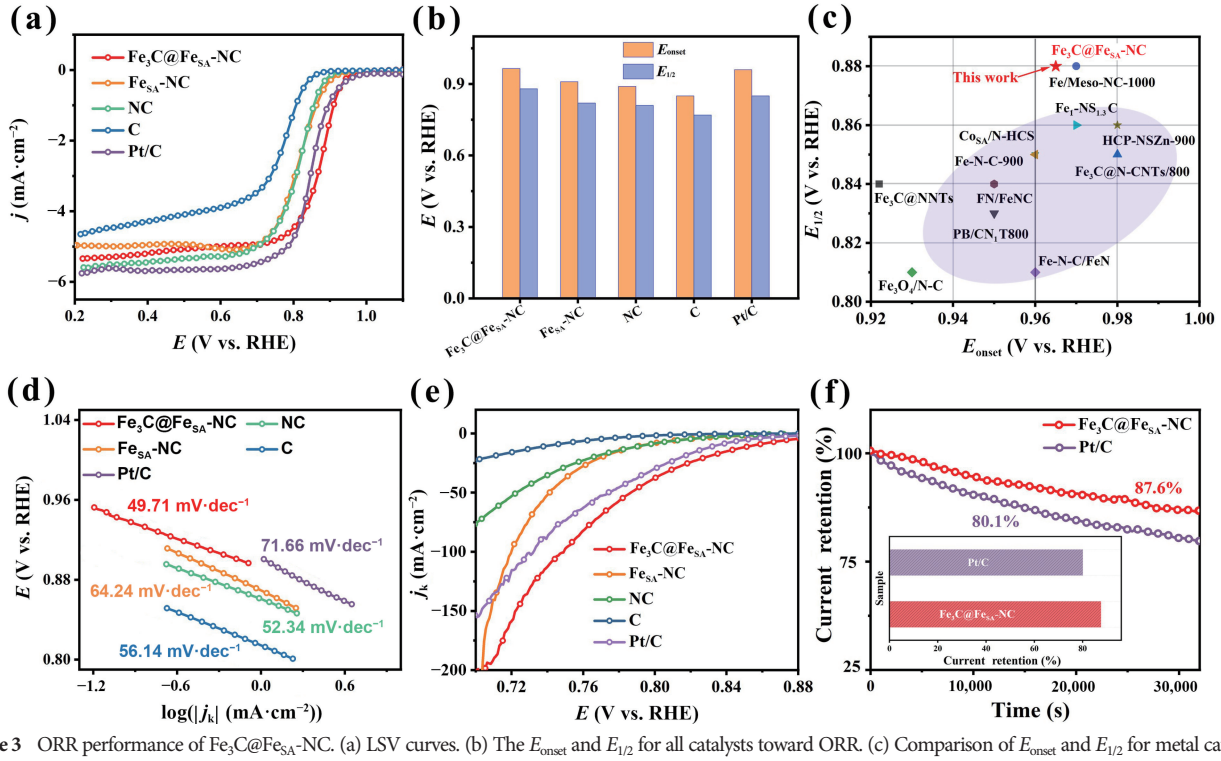

Figure 3 ORR performance of $Fe_3C@Fe_{SA}$-NC. (a) LSV curves. (b) The E_{onset} and $E_{1/2}$ for all catalysts toward ORR. (c) Comparison of E_{onset} and $E_{1/2}$ for metal catalysts in O_2-saturated 0.1 M KOH. (d) The Tafel slopes. (e) The j_k curves of all catalysts. (f) Relative current density–time curves of $Fe_3C@Fe_{SA}$-NC and Pt/C at 0.7 V with a rotation speed of 200 rpm.

retention rate of the original current density for the $Fe_3C@Fe_{SA}$-NC is calculated to be 87.6% (Fig. 3(f)), which is higher than that of 80.1% for commercial Pt/C and comparable to those of other reported M-N-C catalysts in recently reported literatures (Table S3 in the ESM), validating its good ORR stability.

Motivated by its excellent ORR activity, the $Fe_3C@Fe_{SA}$-NC-based ZABs are assembled to evaluate the practical application (Fig. 4(a)). It can be seen in Figs. 4(b) and 4(c) that the ZABs driven by $Fe_3C@Fe_{SA}$-NC own an open circuit potential (OCP) of 1.40 V and a maximum power density of 164.5 mW·cm^{-2}, which are comparable to those of the Pt/C-based ZABs (1.44 V and 112.1 mW·cm^{-2}). The $Fe_3C@Fe_{SA}$-NC-based ZABs display a higher specific capacity of 850.4 mAh·g^{-1} than the Pt/C-based ZABs (550 mAh·g^{-1}) at 10 mA·cm^{-2} (Fig. 4(d)), reaching 78.3% of the theoretical energy density of the ZABs [51]. Furthermore, the ZABs assembled by the $Fe_3C@Fe_{SA}$-NC can power the light-emitting diode (LED) screen for a few hours, indicating the potential practical application ability (Fig. 4(e)). As displayed in Fig. 4(f), the ZABs driven by the $Fe_3C@Fe_{SA}$-NC also pay a voltage of 1.273 V for accomplishing the current density of 1 mA·cm^{-2}, and again return to the 1.265 V when the current density comes back to 1 mA·cm^{-2}. As represented in Fig. 4(g), the ZABs fabricated by the $Fe_3C@Fe_{SA}$-NC show excellent long-term stability over 200 h at a high current density of 50 mA·cm^{-2}, which exceeds the performance of most state-of-the-art ZABs (Table S4 in the ESM). All these results powerfully unveil that the synergistic effect of the single Fe atoms and Fe_3C sites in $Fe_3C@Fe_{SA}$-NC enables it with excellent ORR activities and robust ZABs stability, showcasing the great application prospects in energy conversion devices.

To further reveal the synergistic effect between single Fe atoms and Fe_3C sites on ORR, DFT calculations were performed based on two optimized models including FeN_4 model and Fe_3C + FeN_4 model [11, 52, 53]. As is well known, the ORR process in an alkaline solution involves the complicated protons coupling with electrons steps, in which the protons mainly come from the water dissociation process [11, 19]. The adsorption energies of the $*H_2O$ and $*O_2$ were first calculated on Fe_3C + FeN_4 model, as displayed in Figs. 5(a) and 5(b). The Fe_3C site in Fe_3C + FeN_4 model affords a lower $*H_2O$ adsorption energy (−1.22 eV) and a higher $*O_2$ adsorption energy (−1.71 eV) than the FeN_4 site in this model (−1.03 and −3.56 eV), manifesting the former exhibits the stronger $*H_2O$ adsorption and weaker $*O_2$ adsorption than the latter. Figure 5(c), and Figs. S25 and S26 in the ESM show the Gibbs free energy diagrams of the water dissociation on the Fe_3C site or FeN_4 site in Fe_3C + FeN_4 model, in which the conversion from $*H_2O$ to *OH–H intermediates is recognized as the rate-determining step (RDS). The Fe_3C site in Fe_3C + FeN_4 model requires a lower energy barrier of 2.55 eV toward RDS than the FeN_4 site in this model (2.71 eV), indicating that the Fe_3C site possesses superior water dissociation ability. As displayed in Fig. 5(d), the energy barrier of the protonation process on the Fe_3C site in Fe_3C + FeN_4

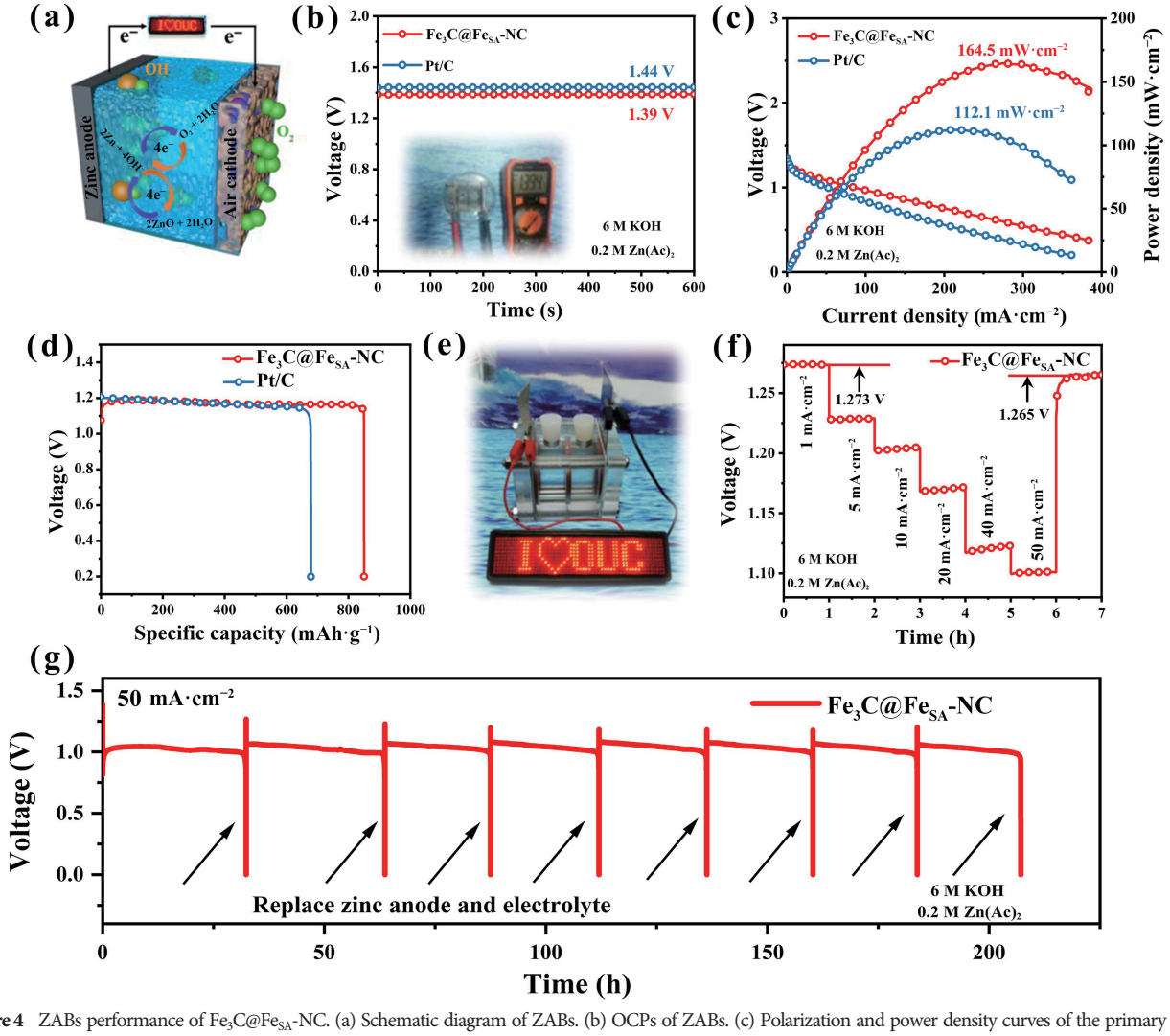

Figure 4 ZABs performance of $Fe_3C@Fe_{SA}$-NC. (a) Schematic diagram of ZABs. (b) OCPs of ZABs. (c) Polarization and power density curves of the primary ZABs. (d) Voltage–capacity curves. (e) Optical picture of a LED screen lighted by $Fe_3C@Fe_{SA}$-NC based ZABs. (f) Galvanostatic discharge curves for primary ZABs at different current densities. (g) Discharge curves for the ZABs at a high current density of 50 mA·cm^{-2}.

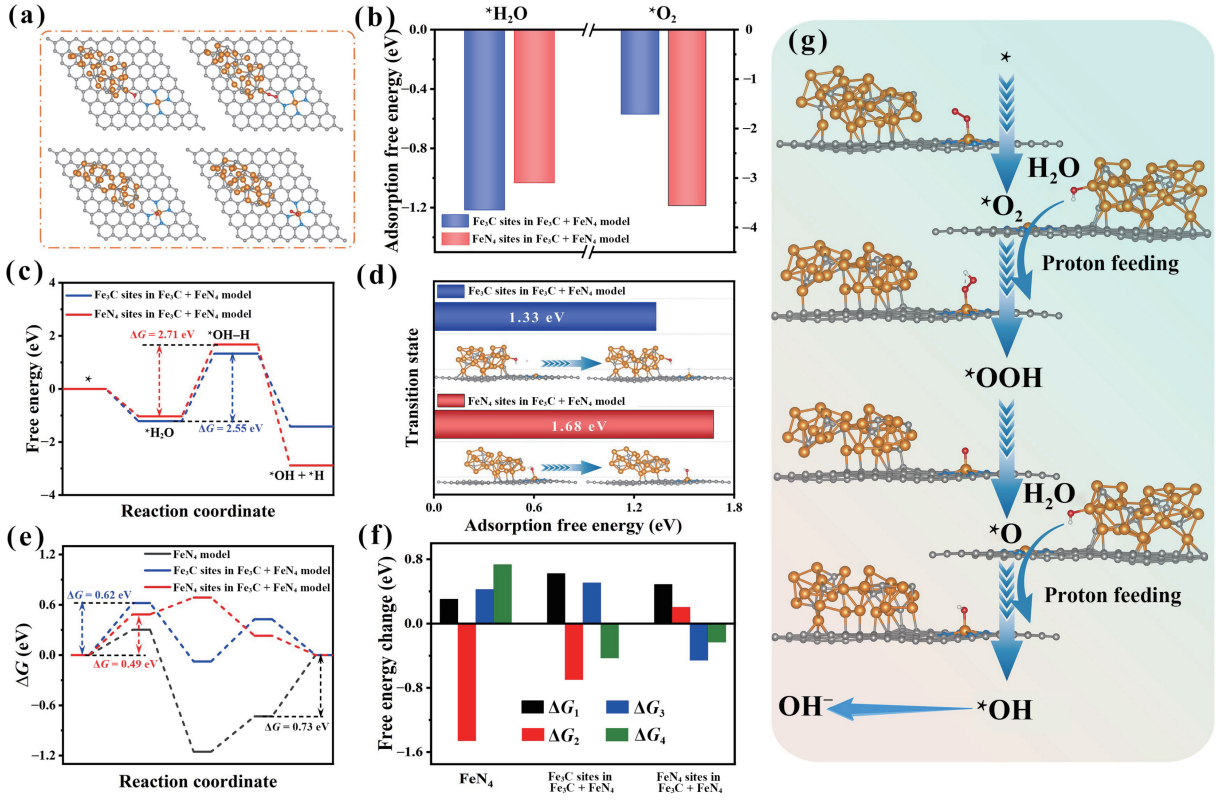

Figure 5 DFT calculations of water dissociation and ORR on FeN_4 and Fe_3C + FeN_4 model. (a) Illustration of representative atomic configurations of the $*H_2O$ and $*O_2$ absorbed on the Fe_3C + FeN_4 model. (b) The E_{ads} of $*H_2O$ and $*O_2$ absorbed on the Fe_3C and FeN_4 sites in Fe_3C + FeN_4 model. (c) Schematic energy diagrams for water dissociation. (d) The energy barrier of the protonation process on the Fe_3C and FeN_4 sites in the Fe_3C + FeN_4 model. (e) ORR free energy diagrams for FeN_4 model (black line), Fe_3C sites in Fe_3C + FeN_4 model (blue line), and FeN_4 sites in Fe_3C + FeN_4 model (red line) at U = 1.23 V. (f) Energy changes for the ORR pathway on the FeN_4 model, Fe_3C sites in Fe_3C + FeN_4 model, and FeN_4 sites in Fe_3C + FeN_4 model (U = 1.23 V). (g) Schematic illustration for water dissociation step and the subsequent elementary processes for ORR in alkaline solutions over the $Fe_3C@Fe_{SA}$-NC electrocatalyst.

model is determined to be 1.33 eV, which is lower than that of the FeN_4 site in Fe_3C + FeN_4 model (1.68 eV), suggesting that the absorbed $*H_2O$ on the Fe_3C sites can more easily produce the proton to participate in the ORR process [54]. Based on the above-mentioned results, the Fe_3C site in Fe_3C + FeN_4 model mainly serves as the active site for the fast water dissociation that could be beneficial to speeding up the supply of protons toward catalyzing ORR. Besides, it can be seen in the Gibbs free diagrams for ORR that all reaction steps are downhill at U = 0 V, indicating the thermodynamic spontaneous process (Figs. S27–S30 in the ESM). When the equilibrium is increased to 1.23 V, the *OH desorption step with the highest uphill free energy (0.73 eV) is the RDS for the ORR process on the pure FeN_4 model (Figs. 5(e) and 5(f)). As for the FeN_4 site in Fe_3C + FeN_4 model, the RDS is the conversion from $*O_2$ to *OOH species that requires an energy barrier of 0.49 eV, which is lower than that of Fe_3C site in Fe_3C + FeN_4 model, demonstrating that the FeN_4 site in Fe_3C + FeN_4 model serves as the active species for ORR. Taken together, one may conclude that the Fe_3C sites in Fe_3C + FeN_4 model mainly serve as the proton-feeding center for speeding up the ORR kinetics of neighboring FeN_4 sites in Fe_3C + FeN_4 model (Fig. 5(g)), which enables the Fe_3C + FeN_4 model with the boosted ORR performance.

4 Conclusions

In conclusion, we have developed an efficient ORR catalyst $Fe_3C@Fe_{SA}$-NC. We found that the strong electronic coupling effect is present between the adjacent Fe_3C nanoparticles and single Fe sites, in which the former represents the fast water dissociation and serves as the proton-feeding centers for boosting the PCET process, and thus resulting in the enhanced ORR kinetics of the latter Fe sites. As a result, the $Fe_3C@Fe_{SA}$-NC affords an excellent half-wave potential of 0.88 V as well as the high kinetic current density, and enables the assembled ZABs with the high peak power density of 164.5 mW·cm^{-2} and long-term stability of over 200 h at high current densities of 50 mA·cm^{-2}. This finding paves the way to design highly efficient and robust electrocatalysts for next-generation metal-air batteries at high current densities.

Acknowledgements

This work was financially supported by the National Natural Science Foundation of China (Nos. 52261145700 and 22279124), the Natural Science Foundation of Shandong Province (No. ZR2020ZD10), and the Fundamental Research Funds for the Central Universities (No. 202262010).

Electronic Supplementary Material: Supplementary material (SEM, TEM, AC HAADF-STEM, electrochemical test, and DFT) is available in the online version of this article at https://doi.org/10.1007/s12274-023-5578-1.

References

[1] Qin, X.; Wang, Z.; Han, J. R.; Luo, Y. L.; Xie, F.; Cui, G.; Guo, X.; Sun, X. Fe-doped CoP nanosheet arrays: An efficient bifunctional catalyst for zinc-air batteries. *Chem. Commun.* **2018**, *54*, 7693–7696.

[2] Wu, J. B.; Su, J. W.; Wu, J.; Huang, L.; Li, Q.; Luo, Y. X.; Jin, H. R.; Zhou, J.; Zhai, T. Y.; Wang, D. S. et al. Scalable synthesis of 2D Mo_2C and thickness-dependent hydrogen evolution on its basal plane and edges. *Adv. Mater.*, in press, https://doi.org/10.1002/adma.202209954.

[3] Li, W. H.; Yang, J. R.; Wang, D. S. Long-range interactions in

diatomic catalysts boosting electrocatalysis. *Angew. Chem., Int. Ed.* **2022**, *134*, e202213318.

[4] Zhang, E. H.; Tao, L.; An, J. K.; Zhang, J. W.; Meng, L. Z.; Zheng, X. B.; Wang, Y.; Li, N.; Du, S. X.; Zhang, J. T. et al. Engineering the local atomic environments of indium single-atom catalysts for efficient electrochemical production of hydrogen peroxide. *Angew. Chem., Int. Ed.* **2022**, *61*, e202117347.

[5] Wang, Y.; Zheng, X. B.; Wang, D. S. Design concept for electrocatalysts. *Nano Res.* **2022**, *15*, 1730–1752.

[6] Zhu, X. F.; Hu, C. G.; Amal, R.; Dai, L. M.; Lu, X. Y. Heteroatom-doped carbon catalysts for zinc-air batteries: Progress, mechanism, and opportunities. *Energy Environ. Sci.* **2020**, *13*, 4536–4563.

[7] Cui, T. T.; Wang, Y. P.; Ye, T.; Wu, J.; Chen, Z. Q.; Li, J.; Lei, Y. P.; Wang, D. S.; Li, Y. D. Engineering dual single-atom sites on 2D ultrathin N-doped carbon nanosheets attaining ultra-low-temperature zinc-air battery. *Angew. Chem., Int. Ed.* **2022**, *61*, e202115219.

[8] Sun, M. Z.; Gong, S. Y.; Zhang, Y. X.; Niu, Z. Q. A perspective on the PGM-free metal-nitrogen-carbon catalysts for PEMFC. *J. Energy Chem.* **2022**, *67*, 250–254.

[9] Wang, Z.; Jin, X. Y.; Zhu, C.; Liu, Y. P.; Tan, H.; Ku, R. Q.; Zhang, Y. Q.; Zhou, L. J.; Liu, Z.; Hwang, S. J. et al. Atomically dispersed Co_2-N_6 and Fe-N_4 costructures boost oxygen reduction reaction in both alkaline and acidic media. *Adv. Mater.* **2021**, *33*, 2104718.

[10] Han, A.; Wang, X. J.; Tang, K.; Zhang, Z. D.; Ye, C. L.; Kong, K. J.; Hu, H. B.; Zheng, L. R.; Jiang, P.; Zhao, C. X. et al. An adjacent atomic platinum site enables single-atom iron with high oxygen reduction reaction performance. *Angew. Chem., Int. Ed.* **2021**, *60*, 19262–19271.

[11] Cao, M. M.; Liu, Y. Y.; Sun, K.; Li, H.; Lin, X. Q.; Zhang, P. X.; Zhou, L. M.; Wang, A.; Mehdi, S.; Wu, X. L. et al. Coupling Fe_3C nanoparticles and N-doping on wood-derived carbon to construct reversible cathode for Zn-air batteries. *Small* **2022**, *18*, 2202014.

[12] Shang, H. S.; Sun, W. M.; Sui, R.; Pei, J. L.; Zheng, L. R.; Dong, J. C.; Jiang, Z. L.; Zhou, D. N.; Zhuang, Z. B.; Chen, W. X. et al. Engineering isolated Mn-N_2C_2 atomic interface sites for efficient bifunctional oxygen reduction and evolution reaction. *Nano Lett.* **2020**, *20*, 5443–5450.

[13] Li, M.; Zhu, H. Y.; Yuan, Q.; Li, T. Y.; Wang, M. M.; Zhang, P.; Zhao, Y. L.; Qin, D. L.; Guo, W. Y.; Liu, B. et al. Proximity electronic effect of Ni/Co diatomic sites for synergistic promotion of electrocatalytic oxygen reduction and hydrogen evolution. *Adv. Funct. Mater.* **2023**, *33*, 2210867.

[14] Wu, J. B.; Xiong, L. K.; Zhao, B. T.; Liu, M. L.; Huang, L. Densely populated single atom catalysts. *Small Methods* **2020**, *4*, 1900540.

[15] Liu, Z. H.; Du, Y.; Yu, R. H.; Zheng, M. B.; Hu, R.; Wu, J. S.; Xia, Y. Y.; Zhuang, Z. C.; Wang, D. S. Tuning mass transport in electrocatalysis down to sub-5 nm through nanoscale grade separation. *Angew. Chem., Int. Ed.* **2023**, *62*, e202212653.

[16] Zhang, P. X.; Liu, Y. Y.; Wang, S. L.; Zhou, L. M.; Liu, T.; Sun, K.; Cao, H. Q.; Jiang, J. C.; Wu, X. L.; Li, B. J. Wood-derived monolithic catalysts with the ability of activating water molecules for oxygen electrocatalysis. *Small* **2022**, *18*, 2202725.

[17] Jiang, R.; Li, Q.; Zheng, X.; Wang, W. Z.; Wang, S. B.; Xu, Z. M.; Wu, J. B. Metal-organic framework-derived Co nanoparticles and single atoms as efficient electrocatalyst for pH universal hydrogen evolution reaction. *Nano Res.* **2022**, *15*, 7917–7924.

[18] Liu, S.; Cheng, H.; Xia, J.; Wang, C.; Gui, R. J.; Zhou, T. P.; Liu, H. F.; Peng, J.; Zhang, N.; Wang, W. J. et al. Surface microenvironment optimization-induced robust oxygen reduction for neutral zinc-air batteries. *Nat. Sci.* **2021**, *1*, e20210005.

[19] Chen, G. B.; Wang, T.; Liu, P.; Liao, Z. Q.; Zhong, H. X.; Wang, G.; Zhang, P. P.; Yu, M. H.; Zschech, E.; Chen, M. W. et al. Promoted oxygen reduction kinetics on nitrogen-doped hierarchically porous carbon by engineering proton-feeding centers. *Energy Environ. Sci.* **2020**, *13*, 2849–2855.

[20] Xiong, Y.; Li, H. C.; Liu, C. W.; Zheng, L. R.; Liu, C.; Wang, J. O.; Liu, S. J.; Han, Y. H.; Gu, L.; Qian, J. S. et al. Single-atom Fe catalysts for Fenton-like reactions: Roles of different N species. *Adv. Mater.* **2022**, *34*, 2110653.

[21] Zhu, P.; Xiong, X.; Wang, D. S. Regulations of active moiety in single atom catalysts for electrochemical hydrogen evolution reaction. *Nano Res.* **2022**, *15*, 5792–5815.

[22] Li, Z. J.; Ji, S. Q.; Xu, C.; Leng, L. P.; Liu, H. X.; Horton, J. H.; Du, L.; Gao, J. C.; He, C.; Qi, X. Y. et al. Engineering the electronic structure of single-atom iron sites with boosted oxygen bifunctional activity for zinc-air batteries. *Adv. Mater.* **2022**, 2209644.

[23] Wu, J. B.; Zhou, H.; Li, Q.; Chen, M.; Wan, J.; Zhang, N.; Xiong, L. K.; Li, S.; Xia, B. Y.; Feng, G. et al. Densely populated isolated single Co-N site for efficient oxygen electrocatalysis. *Adv. Energy Mater.* **2019**, *9*, 1900149.

[24] Jing, H. Y.; Zhu, P.; Zheng, X. B.; Zhang, Z. D.; Wang, D. S.; Li, Y. D. Theory-oriented screening and discovery of advanced energy transformation materials in electrocatalysis. *Adv. Powder Mater.* **2022**, *1*, 100013.

[25] Han, A. L.; Zhang, Z. D.; Yang, J. R.; Wang, D. S.; Li, Y. D. Carbon-supported single-atom catalysts for formic acid oxidation and oxygen reduction reactions. *Small* **2021**, *17*, 2004500.

[26] Feng, W. T.; Cui, Y. P.; Liu, W.; Wang, H. L.; Zhang, Y.; Du, Y. X.; Liu, S.; Wang, H. L.; Gao, X.; Wang, T. Q. Rigid-flexible coupling carbon skeleton and potassium-carbonate-dominated solid electrolyte interface achieving superior potassium-ion storage. *ACS Nano* **2020**, *14*, 4938–4949.

[27] Zhu, Z. J.; Yin, H. J.; Wang, Y.; Chuang, C. H.; Xing, L.; Dong, M. Y.; Lu, Y. R.; Casillas-Garcia, G.; Zheng, Y. L.; Chen, S. et al. Coexisting single-atomic Fe and Ni sites on hierarchically ordered porous carbon as a highly efficient ORR electrocatalyst. *Adv. Mater.* **2020**, *32*, 2004670.

[28] Yao, H. X.; Wang, X. K.; Li, K.; Li, C.; Zhang, C. H.; Zhou, J.; Cao, Z. W.; Wang, H. L.; Gu, M.; Huang, M. H. et al. Strong electronic coupling between ruthenium single atoms and ultrafine nanoclusters enables economical and effective hydrogen production. *Appl. Catal. B: Environ.* **2022**, *312*, 121378.

[29] Zhou, J. Q.; Qian, T.; Yang, T. Z.; Wang, M. F.; Guo, J.; Yan, C. L. Nanomeshes of highly crystalline nitrogen-doped carbon encapsulated Fe/Fe_3C electrodes as ultrafast and stable anodes for Li-ion batteries. *J. Mater. Chem. A* **2015**, *3*, 15008–15014.

[30] Wei, X. Q.; Song, S. J.; Wu, N. N.; Luo, X.; Zheng, L. R.; Jiao, L.; Wang, H. J.; Fang, Q.; Hu, L. Y.; Gu, W. L. et al. Synergistically enhanced single-atomic site Fe by Fe_3C@C for boosted oxygen reduction in neutral electrolyte. *Nano Energy* **2021**, *84*, 105840.

[31] Xu, C. L.; Guo, C. Z.; Liu, J. P.; Hu, B. H.; Dai, J. Y.; Wang, M.; Jin, R.; Luo, Z. L.; Li, H. L.; Chen, C. G. Accelerating the oxygen adsorption kinetics to regulate the oxygen reduction catalysis via Fe_3C nanoparticles coupled with single Fe-N_4 sites. *Energy Storage Mater.* **2022**, *51*, 149–158.

[32] Gao, L.; Zhang, L. L.; Yang, X. L. N,S-codoped porous carbon nanosheets decorated with Fe_3C nanoparticles as high-performance anode materials for lithium ion hybrid supercapacitors. *Rare Met.* **2022**, *41*, 2517–2526.

[33] Yuan, S.; Cui, L. L.; Dou, Z. Y.; Ge, X.; He, X. Q.; Zhang, W.; Asefa, T. Nonprecious bimetallic sites coordinated on N-doped carbons with efficient and durable catalytic activity for oxygen reduction. *Small* **2020**, *16*, 2000742.

[34] Wang, X. K.; Zhou, X. K.; Li, C.; Yao, H. X.; Zhang, C. H.; Zhou, J.; Xu, R.; Chu, L.; Wang, H. L.; Gu, M. et al. Asymmetric Co-N_3P_1 trifunctional catalyst with tailored electronic structures enabling boosted activities and corrosion resistance in an uninterrupted seawater splitting system. *Adv. Mater.* **2022**, *34*, 2204021.

[35] Qiang, F. Q.; Feng, J. G.; Wang, H. L.; Yu, J. H.; Shi, J.; Huang, M. H.; Shi, Z. C.; Liu, S.; Li, P.; Dong, L. F. Oxygen engineering enables N-doped porous carbon nanofibers as oxygen reduction/evolution reaction electrocatalysts for flexible zinc-air batteries. *ACS Catal.* **2022**, *12*, 4002–4015.

[36] Zheng, X. B.; Yang, J. R.; Xu, Z. F.; Wang, Q. S.; Wu, J. B.; Zhang,

E. H.; Dou, S. X.; Sun, W. P.; Wang, D. S.; Li, Y. D. Ru-Co pair sites catalyst boosts the energetics for the oxygen evolution reaction. *Angew. Chem., Int. Ed.* **2022**, *134*, e202205946.

[37] Xiao, M. L.; Chen, Y. T.; Zhu, J. B.; Zhang, H.; Zhao, X.; Gao, L. Q.; Wang, X.; Zhao, J.; Ge, J. J.; Jiang, Z. et al. Climbing the apex of the ORR volcano plot via binuclear site construction: Electronic and geometric engineering. *J. Am. Chem. Soc.* **2019**, *141*, 17763–17770.

[38] Zeng, Z. P.; Gan, L. Y.; Bin Yang, H.; Su, X. Z.; Gao, J. J.; Liu, W.; Matsumoto, H.; Gong, J.; Zhang, J. M.; Cai, W. Z. et al. Orbital coupling of hetero-diatomic nickel-iron site for bifunctional electrocatalysis of CO_2 reduction and oxygen evolution. *Nat. Commun.* **2021**, *12*, 4088.

[39] Cai, S. C.; Cheng, Y. P.; Meng, Z. H.; Li, G. J.; Wu, J. B.; Kan, E. J.; Ouyang, B.; Zhang, H. N.; Tang, H. L. The design of single iron atoms dispersed with nitrogen coordination environment electrocatalyst for zinc-air battery. *J. Power Sources* **2022**, *529*, 231174.

[40] Zhao, S. N.; Li, J. K.; Wang, R.; Cai, J. M.; Zang, S. Q. Electronically and geometrically modified single-atom Fe sites by adjacent Fe nanoparticles for enhanced oxygen reduction. *Adv. Mater.* **2022**, *34*, 2107291.

[41] Dong, Y.; Wang, Y.; Tian, Z. Q.; Jiang, K. M.; Li, Y. L.; Lin, Y. C.; Oloman, C. W.; Gyenge, E. L.; Su, J. W.; Chen, L. Enhanced catalytic performance of Pt by coupling with carbon defects. *Innovation* **2021**, *2*, 100161.

[42] Wang, J. L.; Chen, F. Y.; Jin, Y. C.; Johnston, R. L. Gold-copper aerogels with intriguing surface electronic modulation as highly active and stable electrocatalysts for oxygen reduction and borohydride oxidation. *ChemSusChem* **2018**, *11*, 1354–1364.

[43] Sun, S. F.; Zhou, X.; Cong, B. W.; Hong, W. Z.; Chen, G. Tailoring the d-band centers endows $(Ni_xFe_{1-x})_2P$ nanosheets with efficient oxygen evolution catalysis. *ACS Catal.* **2020**, *10*, 9086–9097.

[44] Zhou, J.; Han, Z. K.; Wang, X. K.; Gai, H. Y.; Chen, Z. K.; Guo, T.; Hou, X. B.; Xu, L. L.; Hu, X. J.; Huang, M. H. et al. Discovery of quantitative electronic structure-OER activity relationship in metal-organic framework electrocatalysts using an integrated theoretical-experimental approach. *Adv. Funct. Mater.* **2021**, *31*, 2102066.

[45] Guo, F. J.; Zhang, M. Y.; Yi, S. C.; Li, X. X.; Xin, R.; Yang, M.; Liu, B.; Chen, H. B.; Li, H. M.; Liu, Y. J. Metal-coordinated porous polydopamine nanospheres derived Fe_3N-FeCo encapsulated N-doped carbon as a highly efficient electrocatalyst for oxygen reduction reaction. *Nano Res. Energy* **2022**, *1*, 9120027.

[46] Li, C.; Zhao, D. H.; Long, H. L.; Li, M. Recent advances in carbonized non-noble metal-organic frameworks for electrochemical catalyst of oxygen reduction reaction. *Rare Met.* **2021**, *40*, 2657–2689.

[47] Gong, S. Y.; Sun, M. Z.; Lee, Y.; Becknell, N.; Zhang, J. W.; Wang, Z. Q.; Zhang, L.; Niu, Z. Q. Bulk-like Pt (100)-oriented ultrathin surface: Combining the merits of single crystals and nanoparticles to boost oxygen reduction reaction. *Angew. Chem., Int. Ed.* **2023**, *62*, e202214516.

[48] Zhou, F. L.; Yu, P.; Sun, F. F.; Zhang, G. Y.; Liu, X.; Wang, L. The cooperation of Fe_3C nanoparticles with isolated single iron atoms to boost the oxygen reduction reaction for Zn-air batteries. *J. Mater. Chem. A* **2021**, *9*, 6831–6840.

[49] Wei, X. Q.; Song, S. J.; Cai, W. W.; Luo, X.; Jiao, L.; Fang, Q.; Wang, X. S.; Wu, N. N.; Luo, Z.; Wang, H. J. et al. Tuning the spin state of Fe single atoms by Pd nanoclusters enables robust oxygen reduction with dissociative pathway. *Chem* **2023**, *9*, 181–197.

[50] Wang, X. K.; Chen, Z. K.; Han, Z. K.; Gai, H. Y.; Zhou, J.; Wang, Y. R.; Cui, P. X.; Ge, J. J.; Xing, W.; Zheng, X. S. et al. Manipulation of new married edge-adjacent Fe_2N_5 catalysts and identification of active species for oxygen reduction in wide pH range. *Adv. Funct. Mater.* **2022**, *32*, 2111835.

[51] Shang, H. S.; Zhou, X. Y.; Dong, J. C.; Li, A.; Zhao, X.; Liu, Q. H.; Lin, Y.; Pei, J. J.; Li, Z.; Jiang, Z. L. et al. Engineering unsymmetrically coordinated $Cu\text{-}S_1N_3$ single atom sites with enhanced oxygen reduction activity. *Nat. Commun.* **2020**, *11*, 3049.

[52] Wang, X. K.; Zhan, G. M.; Wang, Y. R.; Zhang, Y.; Zhou, J.; Xu, R.; Gai, H. Y.; Wang, H. L.; Jiang, H. Q.; Huang, M. H. Engineering core–shell Co_9S_8/Co nanoparticles on reduced graphene oxide: Efficient bifunctional Mott–Schottky electrocatalysts in neutral rechargeable Zn-air batteries. *J. Energy Chem.* **2022**, *68*, 113–123.

[53] Zhang, S. B.; Wu, Y. F.; Zhang, Y. X.; Niu, Z. Q. Dual-atom catalysts: Controllable synthesis and electrocatalytic applications. *Sci. China Chem.* **2021**, *64*, 1908–1922.

[54] Ma, Z. M.; Liu, S. Q.; Tang, N. F.; Song, T.; Motokura, K.; Shen, Z. M.; Yang, Y. Coexistence of Fe nanoclusters boosting Fe single atoms to generate singlet oxygen for efficient aerobic oxidation of primary amines to imines. *ACS Catal.* **2022**, *12*, 5595–5604.